



CrossMark
click for updates

Cite this: *RSC Adv.*, 2016, 6, 45085

Effects of rare earth element doping on the ethanol gas-sensing performance of three-dimensionally ordered macroporous In_2O_3 †

Dongmei Han, Junjun Yang, Fubo Gu and Zhihua Wang*

Rare earth (Tm, Er, La, Yb and Ce)-doped In_2O_3 nanostructures with three-dimensionally ordered macroporous structures (3DOM) were prepared by a colloidal crystal templating method, and their ethanol sensing properties were investigated. Rare earth doping improved the gas response and lowered the optimum operating temperature. Tm-doped 3DOM In_2O_3 had the best gas-sensing performance, and the gas sensitivity for 100 ppm ethanol was seven times higher than that of pure 3DOM In_2O_3 . The reason for the different sensitivities generated by the five doping elements and the underlying mechanism of the enhanced gas response for the samples were studied.

Received 15th March 2016
Accepted 22nd April 2016

DOI: 10.1039/c6ra06816b

www.rsc.org/advances

1. Introduction

In_2O_3 , as an important n-type semiconductor with a wide band gap of about 3.5–3.8 eV,^{1,2} has been used in gas sensors for the detection of various gases, such as NH_3 ,³ NO_2 ,⁴ H_2S ,⁵ ethanol⁶ and formaldehyde.⁷ Recently, some methods have focused on further enhancing the sensitivity of In_2O_3 gas sensors. The recent application of doping has sparked intense research interest in this material due to its effective improvement of electrical conductivity. Doping with metal elements such as Zn,⁸ Sn,⁹ Li,¹⁰ Cr,¹¹ and Cu¹² has been exploited to tailor the gas response properties of In_2O_3 by increasing the free carrier concentration. For example, Li *et al.*¹³ reported Zn-doped In_2O_3 hollow spheres with obviously improved response to Cl_2 . Hu *et al.*¹² synthesized an excellent NO_2 sensor based on Cu-doped In_2O_3 hierarchical flowers.

Rare earth (RE) elements have attracted considerable attention due to their particular characteristics.^{14–17} The high surface basicity, fast oxygen ion mobility and excellent catalytic properties of RE oxides are the important features for chemical sensing.¹⁸ More importantly, RE ions can be easily introduced into the body of In_2O_3 at In^{3+} sites due to their similar ionic radii. The substitution of RE^{3+} ions in the In_2O_3 lattice causes lattice distortion, which results in increased lattice strain.^{19,20} Han *et al.* reported that Ce-doped In_2O_3 porous nanospheres can enhance methanol gas-sensing performance.²¹ Anand *et al.* fabricated Tb-doped In_2O_3 nanoparticles, and the results demonstrated that Tb doping enhanced the response of In_2O_3 towards ethanol.¹⁹ In addition, Er-doped In_2O_3 nanoribbons,²²

La-doped In_2O_3 nanocrystallites,²³ and Eu-doped In_2O_3 nanobelts²⁴ have been investigated as gas sensors. However, the effects of doping with different RE elements on the morphology, crystal structure, crystal defect and gas-sensing properties in the gas-sensing process are not well-understood.

In this investigation, we chose five typical RE elements, Tm, Er, La, Yb and Ce, as dopants to study their effects on the crystal morphology, crystal structure, surface states and gas-sensing response and selectivity. A facile colloidal crystal templating method was used for the fabrication of RE-doped 3DOM In_2O_3 with polymethyl-methacrylate (PMMA) microspheres as a template. The colloidal crystal templating method is a simple and efficient synthetic route for preparing 3DOM materials with well-interconnected pore and wall structures and has attracted considerable attention in recent reports.^{25–27} 3DOM structures can affect the gas response by improving the diffusion and adsorption of gas molecules and accelerating electron exchange between the nanostructure and the target gas. Herein, we found that the sensors based on RE-doped 3DOM In_2O_3 exhibited good sensitivity and selectivity as well as fast response at relatively low temperature for ethanol detection. The gas-sensing mechanism of In_2O_3 nanomaterials and the reason of the widely different enhancement in gas response by the five doping RE elements were discussed.

2. Experimental

2.1. Synthesis of 3DOM In_2O_3 and RE-doped 3DOM In_2O_3

All chemical reagents were analytical grade and used without further purification. The well-arrayed hard-template PMMA microspheres were synthesized according to procedures described elsewhere.²⁸ 3DOM In_2O_3 and RE (Tm, Er, La, Yb, Ce)-doped 3DOM In_2O_3 nanostructures were prepared by a colloidal crystal templating method. $\text{In}(\text{NO}_3)_3 \cdot 4.5\text{H}_2\text{O}$ (10 mmol) and 0.5 mmol $\text{RE}(\text{NO}_3)_3 \cdot y\text{H}_2\text{O}$ (all with purity 99%, RE = Tm, Er, La, Yb,

State Key Laboratory of Chemical Resource Engineering, Beijing University of Chemical Technology, Beijing 100029, P. R. China. E-mail: zhwang@mail.buct.edu.cn

† Electronic supplementary information (ESI) available: The figures of SEM, XRD, XPS and gas-sensing measurements. See DOI: 10.1039/c6ra06816b

Ce) were dispersed into 5 mL of methanol with strong stirring for 1 h. Citric acid (2 g) was added into the mixed solutions under magnetic stirring at room temperature for 1 h. PMMA (1.5 g) was quickly added into the clear solutions and wetted for 4 h. After filtration and drying, the precursors were transferred into a ceramic boat and thermally treated under N_2 flow in a tubular furnace with a flow rate of 50 mL min^{-1} ; the temperature was increased from RT to $300 \text{ }^\circ\text{C}$ at a rate of $1 \text{ }^\circ\text{C min}^{-1}$. The samples were naturally cooled to $50 \text{ }^\circ\text{C}$. After changing the atmosphere to air (flow rate = 100 mL min^{-1}), the temperature was increased $300 \text{ }^\circ\text{C}$ for 3 h and then to $600 \text{ }^\circ\text{C}$ for 3 h (rate = $1 \text{ }^\circ\text{C min}^{-1}$).

Tm, Er, La, Yb and Ce-doped 3DOM In_2O_3 are denoted as 3DOM In_2O_3 -Tm, 3DOM In_2O_3 -Er, 3DOM In_2O_3 -La, 3DOM In_2O_3 -Yb and 3DOM In_2O_3 -Ce, respectively.

2.2. Characterization

The morphologies, sizes and microstructures of the samples were studied using scanning electron microscopy (SEM, S-4700) and transmission electron microscopy TEM (H-800). Powder X-ray diffraction (XRD; Bruker/AXS D8 Advance) with $\text{Cu K}\alpha$ radiation ($\lambda = 0.15406 \text{ nm}$) and a nickel filter was used to measure the crystal structures of the samples at a scan rate of $10^\circ \text{ min}^{-1}$ with a scope of $5\text{--}90^\circ$. The crystal phases were identified by the JCPDS Database. The chemical characteristics and elemental compositions of the samples were examined by energy dispersive spectroscopy (EDS; S-4700). X-ray photoelectron spectroscopy (XPS, VG Scientific ESCALAB 250X) with $\text{Al K}\alpha$ excitation was used to characterize the RE and indium species and surface properties.

2.3. Gas sensing measurements

A CGS-8TP (Beijing Elite Tech. Co., Ltd, China) gas-sensing intelligent system was used to test the sensing properties of the sensors. The relative humidity range of the testing environment was $25 \pm 5\%$. The obtained samples were mixed with ethanol to form a homogeneous paste, which was coated on an alumina ceramic tube with a pair of Au electrodes and four Pt

wires on both ends of the tube, and aged at $300 \text{ }^\circ\text{C}$ for 24 h in air in a muffle furnace. The ceramic tube was then welded on a substrate, and a Ni-Cr wire coil throughout the tube served as the heater to control the working temperature by varying the heating current. The sensor's sensitivity to gas was defined as R_a/R_g , where R_g is the resistance of the sensor in the target gas, and R_a is the resistance in air. The response time of the sensor is defined as the time taken by the sensor to reach 90% of its maximum value after exposure to test gas, and the recovery time is the time taken for the sensor to reach 10% of its original resistance value once the desorption begins. A schematic illustration of the experimental procedure is shown in Fig. 1.

3. Results and discussion

3.1. Characterization of pure and RE-doped 3DOM In_2O_3

The SEM images of PMMA microspheres with an average diameter 300 nm are shown in Fig. S1.† The influence of calcination temperature on the morphology of 3DOM In_2O_3 is shown in Fig. S2.† The PMMA templates were not completely degraded, and the channel structure was not obvious for 3DOM In_2O_3 annealed at $550 \text{ }^\circ\text{C}$ (Fig. S2a and b†). For 3DOM In_2O_3 annealed at $600 \text{ }^\circ\text{C}$ (Fig. S2c and d†), the walls of the 3DOM regular arrays were complete, and the channel structure was obvious. However, at an annealing temperature of $650 \text{ }^\circ\text{C}$ (Fig. 2e and f), the channel structure and the walls of the 3DOM structure were slightly damaged. Therefore, the 3DOM In_2O_3 samples were prepared at $600 \text{ }^\circ\text{C}$ for further study.

The 3DOM In_2O_3 materials had ordered macroporous hierarchical structures with an average pore diameter of $\sim 200 \text{ nm}$ and wall thickness of $\sim 25 \text{ nm}$ (Fig. 2a and b), corresponding to a shrinkage of 30% compared to the initial size (*ca.* $\sim 300 \text{ nm}$) of the PMMA microspheres. The samples annealed at $600 \text{ }^\circ\text{C}$ presented hexagonal structures with regular lamination.^{29,30} The structures of all the RE-doped 3DOM In_2O_3 were similar to the structure of 3DOM In_2O_3 , and the RE doping did not destroy the regular structure. The average pore diameters of the RE-doped 3DOM In_2O_3 were all approximately 200 nm , and the wall thicknesses were 25 nm . In order to further observe the

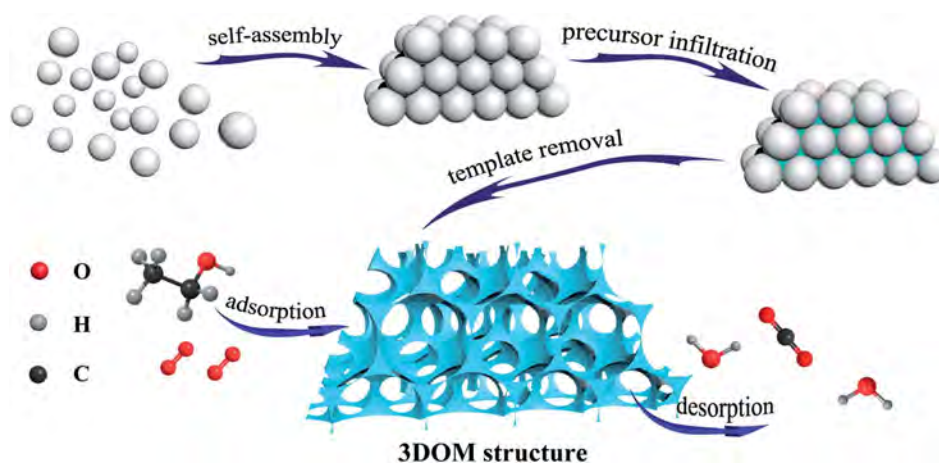


Fig. 1 Schematic illustration of the experimental procedure for the preparation of 3DOM In_2O_3 materials.

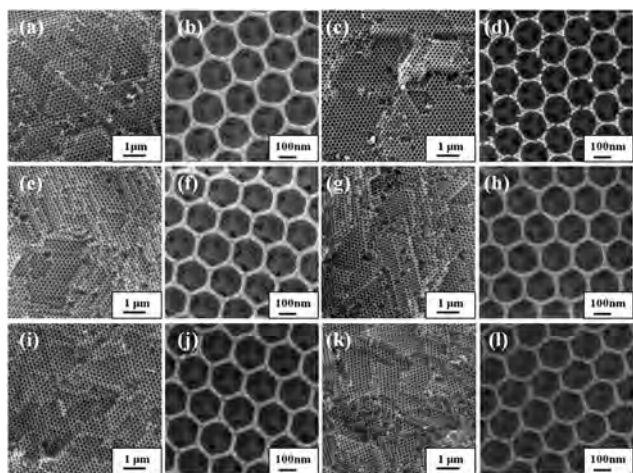


Fig. 2 SEM images of 3DOM In_2O_3 (a, b); 3DOM $\text{In}_2\text{O}_3\text{-Tm}$ (c, d); 3DOM $\text{In}_2\text{O}_3\text{-Er}$ (e, f); 3DOM $\text{In}_2\text{O}_3\text{-La}$ (g, h); 3DOM $\text{In}_2\text{O}_3\text{-Yb}$ (i, j); and 3DOM $\text{In}_2\text{O}_3\text{-Ce}$ (k, l).

microscopic structures of the 3DOM materials, TEM was applied to analyze the RE-doped 3DOM In_2O_3 materials. Fig. 3 shows the complete skeleton structure at higher magnification to reveal more details. All 3DOM structures retained ordered macroporous structures, and the skeletons were assembled out of In_2O_3 nanoparticles to form a wall thickness of 18–25 nm. No remarkable change in surface morphology was observed among these samples, which may be attributed to the two following reasons. First, these RE elements possess comparable ionic radii [In^{3+} (0.80 Å), La^{3+} (1.06 Å), Ce^{3+} (1.03 Å), Er^{3+} (0.88 Å), Tm^{3+} (0.87 Å), Yb^{3+} (0.86 Å)], and In^{3+} is substituted by RE ions without a change in the crystal structure of In_2O_3 .^{31,32} Second, the relatively low concentration of RE dopants³³ in this work may not significantly change the morphology of the as fabricated sample.

Fig. 4a shows the XRD patterns of the pure and RE-doped 3DOM In_2O_3 samples. The samples were identical to the cubic crystal In_2O_3 samples with lattice parameter $a = 10.12$ Å (JCPDS PDF# 06-0416; Fig. S3†). The main peaks at 30.5° , 35.4° , 51.0°

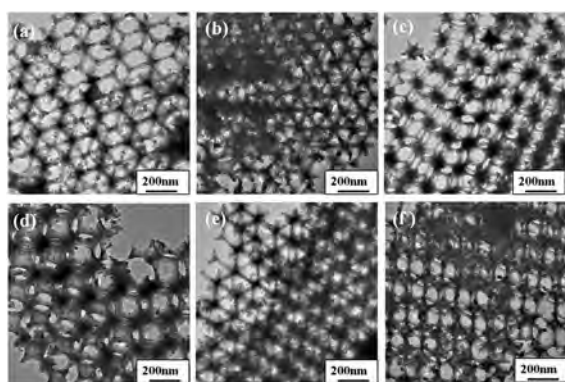


Fig. 3 TEM images of (a) 3DOM In_2O_3 ; (b) 3DOM $\text{In}_2\text{O}_3\text{-Tm}$; (c) 3DOM $\text{In}_2\text{O}_3\text{-Er}$; (d) 3DOM $\text{In}_2\text{O}_3\text{-La}$; (e) 3DOM $\text{In}_2\text{O}_3\text{-Yb}$; (f) 3DOM $\text{In}_2\text{O}_3\text{-Ce}$.

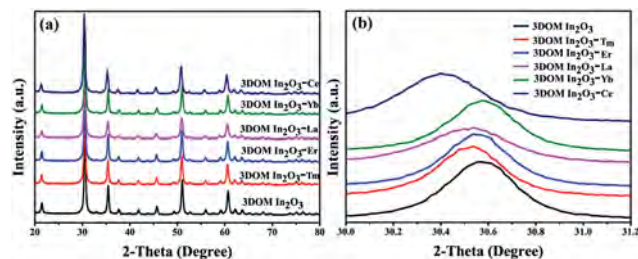


Fig. 4 XRD patterns of (a) the pure and RE-doped 3DOM In_2O_3 samples and (b) high magnification of the (222) XRD peaks.

and 60.7° correspond to the (222), (400), (440) and (622) lattice planes, respectively, indicating that samples with well-defined crystallites were obtained.^{34,35} For the RE-doped 3DOM In_2O_3 , no diffraction peaks of RE were observed. The (222) diffraction peaks of RE-doped samples were shifted slightly towards lower 2θ values compared with pure In_2O_3 (Fig. 4b), suggesting that structural defects in In_2O_3 were caused by the RE dopants.^{36,37} The difference in ionic radius leads to the deformation of the In_2O_3 crystal lattice. Because the radii of RE^{x+} are larger than that of In^{3+} , doping with the RE^{x+} will lead to the lattice distortion of In_2O_3 , restrain the crystal grain growth, and eventually cause significant lattice deformation. The diameters of six kinds of crystals were determined by the Debye–Scherrer formula, and the lattice constants were calculated from the XRD peaks. The calculated values are listed in Table 1. The results indicate that the lattice constant increased when the RE ions were substituted at In^{3+} sites. Basis on the above XRD analysis, it can be concluded that RE^{3+} ions uniformly substitute at In^{3+} sites.^{38,39}

The elemental composition can be determined precisely using EDS. The RE-doped samples consisted of elemental In, O and doped RE element (Tm or Er, La, Yb, Ce; Fig. 5a–f). According to the EDS analysis, the actual ratio of RE to In was about 0.041–0.055, which is close to the proposed doping concentration. The maximum value of the In peak was 11.31 K at 3.3 keV. The In peak values of 3DOM In_2O_3 doped with Tm, Er, La, Yb, and Ce were 6.74 K, 7.43 K, 7.60 K and 6.92 K and 6.26 K, respectively, which are distinctly lower than those of pure 3DOM In_2O_3 .

The XRD and EDS results indicate that RE^{x+} ions were successfully doped into the crystal lattice of the In_2O_3 matrix without forming RE oxides or any other impurities.

XPS analysis was conducted to confirm the change in the amount of defects at the surface of In_2O_3 caused by RE doping. The survey XPS spectra of the samples are shown in Fig. S4(a–f†). C, In and O elements were present in all the spectra. For the pure 3DOM In_2O_3 , the peaks centered at 703.0, 665.7, 450.96 and 443.91 eV are assigned to $\text{In } 3p_{1/2}$, $\text{In } 2p_{3/2}$, $3d_{3/2}$ and $\text{In } 3d_{5/2}$, respectively, suggesting that In only existed in the trivalent oxidation state in the samples.⁴⁰ No significant changes were observed in the full-range survey XPS spectra of the RE-doped 3DOM In_2O_3 due to the low content of doped RE ions.

Furthermore, compared with pure 3DOM In_2O_3 , the binding energies of the In 3d XPS peaks of the RE-doped 3DOM In_2O_3

Table 1 Crystal size, lattice parameters and doping ratio of pure and RE-doped 3DOM In_2O_3

Samples	Crystal size ^a (nm)	Lattice parameters ^a $a = b = c$ (Å)	RE/In ^b (mol%)
3DOM In_2O_3	22.2448	10.1200	—
3DOM In_2O_3 -Tm	21.9386	10.1326	4.8
3DOM In_2O_3 -Er	22.1375	10.1294	4.5
3DOM In_2O_3 -La	18.3579	10.1373	4.1
3DOM In_2O_3 -Yb	21.6361	10.1210	5.4
3DOM In_2O_3 -Ce	18.8294	10.1685	5.4

^a Determined by XRD. ^b Determined by EDS.

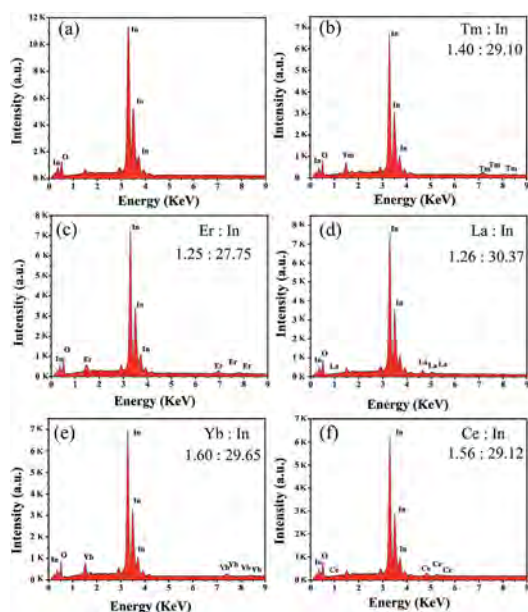


Fig. 5 EDS patterns of the (a) 3DOM In_2O_3 ; (b) 3DOM In_2O_3 -Tm; (c) 3DOM In_2O_3 -Er; (d) 3DOM In_2O_3 -La; (e) 3DOM In_2O_3 -Yb; and (f) 3DOM In_2O_3 -Ce samples.

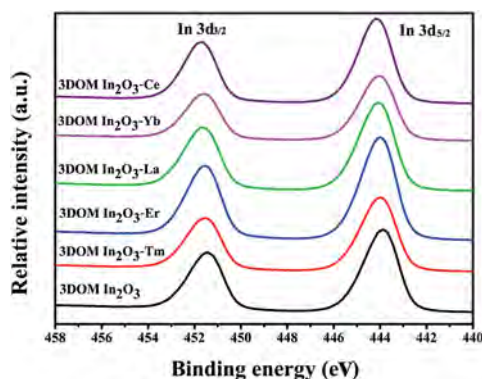


Fig. 6 In 3d XPS spectra of pure and RE-doped 3DOM In_2O_3 .

shifted to higher values, as shown in Fig. 6. This phenomenon indicates that an electronic interaction existed between In_2O_3 and the dopants. In Fig. 3(b–f), the peaks located at 176.44, 168.74, 838.52, 184.77 and 884.85 eV belong to the Tm 4d, Er 4d, La 3d_{5/2}, Yb 4d and Ce 3d_{5/2} peaks, respectively; these peaks

were found at higher energies than those of the pure RE oxide, further verifying that the RE elements were successfully doped into the In_2O_3 lattice.²⁰

3.2. Gas sensing properties and sensing mechanism

The gas-sensing properties of 3DOM In_2O_3 with different doping ratios of RE elements were measured in our experiments, and trends were observed among the different elements. Taking Tm as an example, the gas-sensing properties of 3DOM In_2O_3 with 2%, 5%, and 8% doping ratios are shown in Fig. S5.† The experimental results indicated that the optimum performance can be achieved with a Tm doping ratio of 5%.

The gas response usually depends on the working temperature of the sensor. Fig. 7a shows the gas responses to 100 ppm ethanol measured at different operating temperatures for pure and RE-doped 3DOM In_2O_3 . The optimum working temperature of 3DOM In_2O_3 decreased from 230 °C to 175 °C by doping with RE elements. The responses of all the RE-doped 3DOM In_2O_3 were dramatically higher than that of 3DOM In_2O_3 at 175 °C. The 3DOM In_2O_3 -Tm had the best gas-sensing property followed by 3DOM In_2O_3 -Er, 3DOM In_2O_3 -La, 3DOM In_2O_3 -Yb, 3DOM In_2O_3 -Ce and pure 3DOM In_2O_3 . The results indicated that RE doping is an efficient way to improve the gas response of semiconductor-based gas sensors. It is worth noting that the gas sensitivity of the 3DOM In_2O_3 -Tm was seven times higher than that of pure In_2O_3 .

The gas responses and response/recovery times of the pure and RE-doped 3DOM In_2O_3 are shown in Fig. S6 and S7.† RE-doped 3DOM In_2O_3 exhibited a fast response time (~9 s), fast recovery time (~13 s) and high gas response for 100 ppm ethanol. The dynamic response curves for various concentrations of ethanol for all samples are shown in Fig. 7b. The gas responses were gradually enhanced with increasing ethanol concentration. The linear relationship between gas response and ethanol concentration was good (in the range of 20–100 ppm) for all samples (Fig. 7c). Upon further increases in the concentration of ethanol, the increasing rate of gas response reduces, as shown in Fig. S8.†

Good selectivity is required for practical applications of gas sensors. Therefore, the responses of the pure and RE-doped 3DOM In_2O_3 to 100 ppm methanol (CH_3OH), acetone ($\text{C}_3\text{H}_6\text{O}$), ammonia (NH_3) and cyclohexane (C_6H_{12}) were measured at 175 °C, as shown in Fig. 8a. The responses of all samples for other

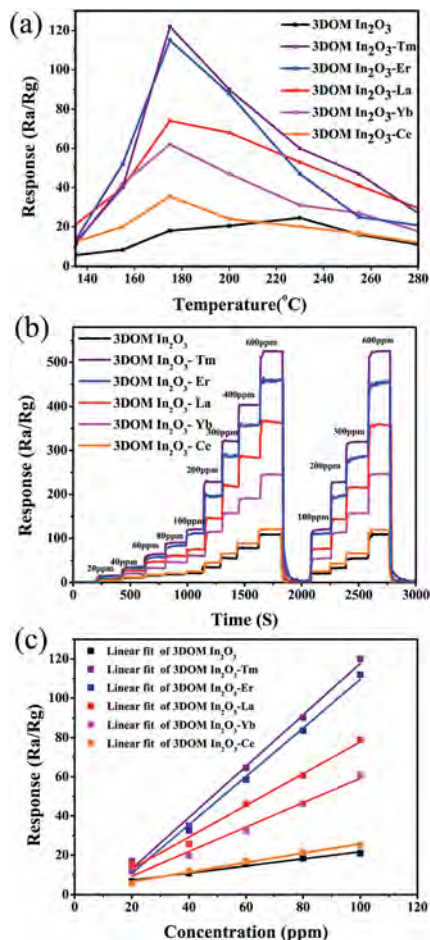


Fig. 7 (a) Gas responses of pure and RE-doped 3DOM In₂O₃ to 100 ppm ethanol at different operating temperatures. (b) Dynamic response curves and (c) linear relationship responses of pure and RE-doped 3DOM In₂O₃ to different concentrations of ethanol.

gases were very low, indicating that the RE-doped 3DOM In₂O₃ samples in this work had very good selectivities for ethanol.

In practice, the stability is also a critical factor for sensors. Stability tests were carried out for the sensors in air for 10 days, 30 days and 60 days, as shown in Fig. 8b. Even after 60 days, the samples still had good responses, and no obvious changes were observed in their gas-sensing properties. A comparison of different In₂O₃-based sensors for ethanol detection is given in Table 2. The Tm-, Er- and La-doped 3DOM In₂O₃ samples exhibited higher gas responses and lower optimum working temperatures than other materials reported in the literature.

The surface structure is an important factor that influences the gas-sensing properties. XPS analysis was carried out to explore the differences in gas-sensing properties among the samples. The Gauss fitting curves of the 1s XPS spectra of the pure and RE-doped 3DOM In₂O₃ samples are shown in Fig. 9. Three peaks centered at 529.50 eV (OI), 531.04 eV (OII) and 532.29 eV (OIII) are assigned to OI, OII and OIII species, respectively.^{45–47} The OI species belongs to lattice oxygen, the OII species is attributed to adsorbed oxygen (O₂⁻, O⁻ and O²⁻ ions) species, and the OIII species is assigned to hydroxyl oxygen.

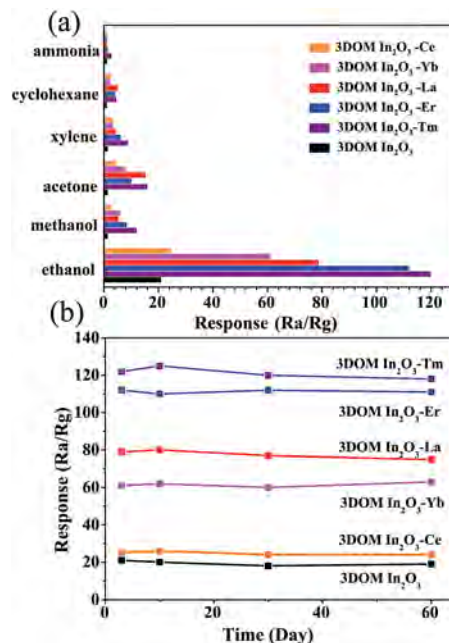


Fig. 8 (a) Selectivity of pure and RE-doped 3DOM In₂O₃ to 100 ppm of different gases under the optimum working temperature. (b) Sensing stability to 100 ppm of ethanol for nearly two months.

Table 2 Comparison of the responses of In₂O₃ nanostructures to ethanol

Sample structure	<i>T</i> /°C	Concentration/ ppm	Response	Reference
3DOM In ₂ O ₃ -Tm	175	100	122	Present work
3DOM In ₂ O ₃ -Er	175	100	112	Present work
3DOM In ₂ O ₃ -La	175	100	78.9	Present work
Ga ₂ O ₃ -In ₂ O ₃ nanocomposite	300	300	69.1	41
Cr ₂ O ₃ decorated In ₂ O ₃	200	500	15.03	42
CuO/In ₂ O ₃ core-shell nanorods	300	200	7.26	43
Bi ₂ O ₃ decorated In ₂ O ₃	200	200	17.74	44
Tb doped In ₂ O ₃ nanoparticles	300	50	40	19

The adsorbed oxygen contents are important for the gas-sensing properties. OII species are advantageous for the ethanol decomposition reaction on the sensor surface, which is beneficial to the gas response. The relative amounts of oxygen species calculated from the O 1s XPS spectra are listed in Table 3. 3DOM In₂O₃-Tm clearly had the highest relative amount of OII followed by 3DOM In₂O₃-Er, 3DOM In₂O₃-La, 3DOM In₂O₃-Yb, 3DOM In₂O₃-Ce and pure 3DOM In₂O₃. Based on the gas-sensing performances and O 1s XPS results, we can conclude that OII is the main factor affecting the gas response, and the sensor performance can be improved by increasing the amount of adsorbed oxygen. The 3DOM In₂O₃-Tm with the largest relative amount of adsorbed oxygen exhibited the highest gas sensitivity, and the amount of adsorbed oxygen of RE-

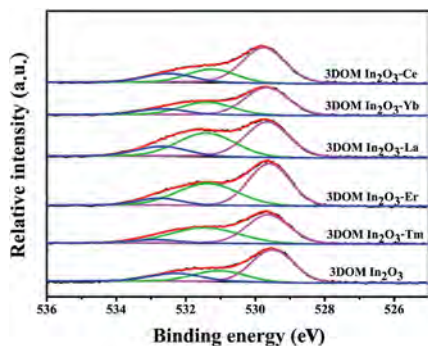


Fig. 9 O 1s XPS spectra of pure and RE-doped 3DOM In_2O_3 .

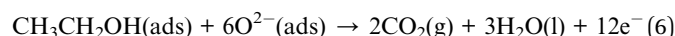
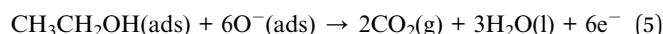
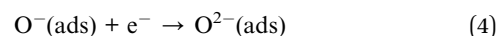
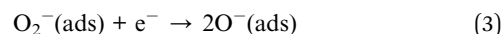
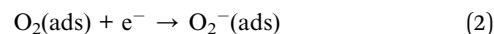
Table 3 Data from the O 1s Gauss fittings of pure and RE-doped 3DOM In_2O_3

Samples	OI (%)	OII (%)	OIII (%)
3DOM In_2O_3	58.97	23.81	17.22
3DOM In_2O_3 -Tm	51.50	42.34	6.16
3DOM In_2O_3 -Er	51.66	39.61	8.73
3DOM In_2O_3 -La	48.15	38.10	13.75
3DOM In_2O_3 -Yb	57.37	30.34	12.29
3DOM In_2O_3 -Ce	58.61	24.54	16.85

doped 3DOM In_2O_3 is larger than that of the pure 3DOM In_2O_3 . Therefore, the XPS analysis provided a satisfactory explanation for the difference in gas-sensing properties obtained using the 3DOM In_2O_3 samples doped with different elements.

The gas-sensing mechanism of the In_2O_3 sensors can be explained by a surface-depletion model. When the sensors are exposed to air, the oxygen molecules will be adsorbed on the

surface of In_2O_3 to capture electrons from the conduction band and form adsorbed oxygen species (O_2^- , O^{2-} and O^-),^{48–50} as represented in eqn (1)–(4). At the same time, a thick space-charge layer is formed on the surface of In_2O_3 , increasing the potential barrier with a higher resistance. As previously mentioned, Tm-doped 3DOM In_2O_3 had the highest amount of OII species, meaning that it can adsorb the most oxygen molecules among all the RE-doped samples. This leads to the most electrons being extracted on the surface and the widest space-charge layers being formed (shown in Fig. 10). Consequently, the initial resistance (R_a) will increase. Along with the relative amount of OII species decreasing gradually from Er to Ce, the width of the space-charge layer decreases in sequence.



As shown in eqn (5) and (6), when the In_2O_3 sensors are exposed to ethanol, the oxygen species will react with ethanol and simultaneously release the trapped electrons back to the conduction band, finally reducing the thickness of the electron depletion layer. Accordingly, the resistance of In_2O_3 semiconductor materials will decrease. 3DOM In_2O_3 -Tm, which has the most adsorbed oxygen, has the strongest reaction with

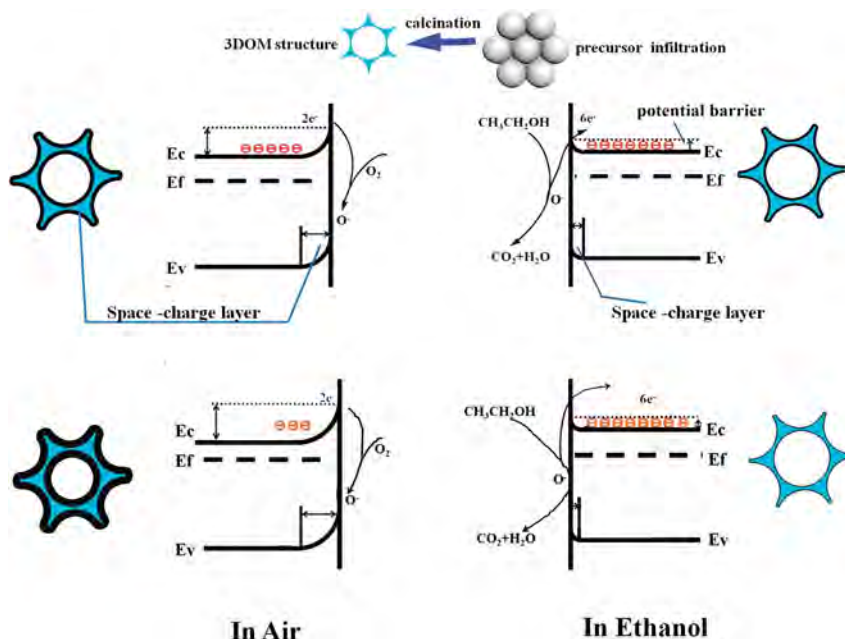


Fig. 10 Schematic illustration of the gas-sensing mechanism (E_v , valence band edge; E_c , conduction band edge; E_f , Fermi energy).

ethanol and releases more electrons than other samples. 3DOM In₂O₃-Tm has the best gas performance, with the most obvious change of resistance followed by 3DOM In₂O₃-Er, 3DOM In₂O₃-La, 3DOM In₂O₃-Yb, and 3DOM In₂O₃-Ce.

4. Conclusions

RE-doped 3DOM In₂O₃ samples were prepared by a colloidal crystal templating method. The 3DOM framework provided greater opportunity for the adsorption of reactants on the surfaces of the sensors. Compared with pure 3DOM In₂O₃, the optimum working temperature of the RE-doped 3DOM In₂O₃ samples were lower, and the gas responses were enhanced. 3DOM In₂O₃-Tm had the highest relative amount of OII species and showed the highest gas response, which was seven times higher than that of pure 3DOM In₂O₃. Moreover, RE-doped 3DOM In₂O₃ exhibited good stability and high selectivity for ethanol. RE doping improved the oxygen absorption and consequently broadened the electron depletion on the surface, ultimately enhancing the gas-sensing performance. Therefore, RE-doped 3DOM In₂O₃ macroporous materials are expected to have promising applications in the field of ethanol detection.

Acknowledgements

The authors acknowledge the National Natural Science Foundation of China (No. 21275016 and 21575011).

Notes and references

- 1 F. R. Li, J. K. Jian, R. Wu, J. Li and Y. F. Sun, *J. Alloys Compd.*, 2015, **645**, 178–183.
- 2 M. Jothibas, C. Manoharan, S. Johnson Jeyakumar and P. Praveen, *J. Mater. Sci.: Mater. Electron.*, 2015, **26**, 9600–9606.
- 3 D. J. Lee, J. Park, H. S. Kim, D. H. Lee, M. Park, H. Chang, J. H. Jin, J. R. Sohn, K. Heo and B. Y. Lee, *Sens. Actuators, B*, 2015, **216**, 482–487.
- 4 L. P. Gao, Z. X. Cheng, Q. Xiang, Y. Zhang and J. Q. Xu, *Sens. Actuators, B*, 2015, **208**, 436–443.
- 5 W. Zheng, X. F. Lu, W. Wang, Z. Y. Li, H. N. Zhang, Z. J. Wang, X. R. Xu, S. Y. Li and C. Wang, *J. Colloid Interface Sci.*, 2009, **338**, 366–370.
- 6 X. G. Han, X. Han, L. Q. Sun, S. G. Gao, L. Li, Q. Kuang, Z. Q. Xie and C. Wang, *Chem. Commun.*, 2015, **51**, 9612–9615.
- 7 F. Fang, L. Bai, H. Y. Sun, Y. Kuang, X. M. Sun, T. Shi, D. S. Song, P. Guo, H. P. Yang, Z. F. Zhang, Y. Wang, J. Luo and J. Zhu, *Sens. Actuators, B*, 2015, **206**, 714–720.
- 8 P. Li, H. Q. Fan, Y. Cai, M. M. Xu, C. B. Long, M. M. Li, S. H. Lei and X. W. Zou, *RSC Adv.*, 2014, **4**, 15161–15170.
- 9 A. Ayeshamariam, M. Kashif, M. Bououdina, U. Hashim, M. Jayachandran and M. E. Ali, *Ceram. Int.*, 2014, **40**, 1321–1328.
- 10 N. G. Pramod and S. N. Pandey, *Ceram. Int.*, 2015, **41**, 527–532.
- 11 S. Park, S. Kim, G. L. Sun, S. Choi, S. Lee and C. Lee, *Ceram. Int.*, 2015, **41**, 9823–9827.
- 12 X. L. Hu, L. Y. Tian, H. B. Sun, B. Wang, Y. Gao, P. Sun, F. M. Liu and G. Y. Lu, *Sens. Actuators, B*, 2015, **221**, 297–304.
- 13 P. Li and H. Q. Fan, *CrystEngComm*, 2014, **16**, 2715–2722.
- 14 P. Pandey, R. Kurchania and F. Z. Haque, *Opt. Spectrosc.*, 2015, **119**, 666–671.
- 15 A. Marsal, A. Cornet and J. R. Morante, *Sens. Actuators, B*, 2003, **94**, 324–329.
- 16 I. T. Weber, A. Valentini, L. F. D. Probst, E. Longo and E. R. Leite, *Mater. Lett.*, 2008, **62**, 1677–1680.
- 17 Y. Xiong, G. Z. Zhang, D. W. Zeng and C. S. Xie, *Mater. Res. Bull.*, 2014, **52**, 56–64.
- 18 G. Singh, R. Thangaraj and R. C. Singh, *Ceram. Int.*, 2016, **42**, 4323–4332.
- 19 K. Anand, J. Kaur, R. C. Singh and R. Thangaraj, *Mater. Sci. Semicond. Process.*, 2015, **39**, 476–483.
- 20 Z. H. Wang, Z. W. Tian, D. M. Han and F. B. Gu, *ACS Appl. Mater. Interfaces*, 2016, **8**, 5466–5474.
- 21 D. Han, P. Song, S. Zhang, H. H. Zhang, Q. Xu and Q. Wang, *Sens. Actuators, B*, 2015, **216**, 488–496.
- 22 Z. J. Qin, Y. K. Liu, W. W. Chen, P. Ai, Y. M. Wu, S. H. Li and D. P. Yu, *Chem. Phys. Lett.*, 2016, **646**, 12–17.
- 23 V. D. Kapse, S. A. Ghosh, G. N. Chaudhari, F. C. Raghuvanshi and D. D. Gulwade, *Vacuum*, 2008, **83**, 346–352.
- 24 W. W. Chen, Y. K. Liu, Z. J. Qin, Y. M. Wu, S. H. Li and P. Ai, *Sensors*, 2015, **15**, 29950–29957.
- 25 L. J. Wang, H. L. Fan, S. G. Ju, E. Croiset, Z. W. Chen, H. Wang and J. Mi, *ACS Appl. Mater. Interfaces*, 2014, **6**, 21167–21177.
- 26 L. Lu and A. Eychmüller, *Acc. Chem. Res.*, 2008, **41**, 244–253.
- 27 H. Arandiyani, J. Scott, Y. Wang, H. Dai, H. X. Sun and R. Amal, *ACS Appl. Mater. Interfaces*, 2016, **8**, 2457–2463.
- 28 Y. X. Liu, H. X. Dai, J. G. Deng, X. W. Li, Y. Wang, H. Arandiyani, S. H. Xie, H. G. Yang and G. S. Guo, *J. Catal.*, 2013, **305**, 146–153.
- 29 H. Arandiyani, H. X. Dai, K. M. Ji, H. Y. Sun and J. H. Li, *ACS Catal.*, 2015, **5**, 1781–1793.
- 30 M. Zhou, J. Bao, Y. Xu, J. J. Zhang, J. F. Xie, M. L. Guan, C. L. Wang, L. Y. Wen, Y. Lei and Y. Xie, *ACS Nano*, 2014, **8**, 7088–7098.
- 31 A. S. Ahmed, S. M. Muhamed, M. L. Singla, S. Tabassum, A. H. Naqvi and A. Azam, *J. Lumin.*, 2011, **131**, 1–6.
- 32 C. Stella, N. Soundararajan and K. Ramachandran, *J. Mater. Sci.: Mater. Electron.*, 2015, **26**, 4178–4184.
- 33 B. Y. Huang, C. H. Zhao, M. X. Zhang, Z. M. Zhang, E. Q. Xie, J. Y. Zhou and W. H. Han, *Appl. Surf. Sci.*, 2015, **349**, 615–621.
- 34 F. L. Gong, H. Z. Liu, C. Y. Liu, Y. Y. Gong, Y. H. Zhang, E. C. Meng and F. Li, *Mater. Lett.*, 2016, **163**, 236–239.
- 35 H. F. Yang, X. Zhang, J. F. Li, W. T. Li, G. S. Xi, Y. Yan and H. Bai, *Microporous Mesoporous Mater.*, 2014, **200**, 140–144.
- 36 J. Liu, W. B. Guo, F. D. Qu, C. H. Feng, C. Li, L. H. Zhu, J. R. Zhou, S. P. Ruan and W. Y. Chen, *Ceram. Int.*, 2014, **40**, 6685–6689.
- 37 L. Xu, B. Dong, Y. Wang, X. Bai, J. S. Chen, Q. Liu and H. W. Song, *J. Phys. Chem. C*, 2010, **114**, 9089–9095.
- 38 B. Y. Huang, C. H. Zhao, M. X. Zhang, Z. M. Zhang, E. Q. Xie, J. Y. Zhou and W. H. Han, *Appl. Surf. Sci.*, 2015, **349**, 615–621.

- 39 C. H. Zhao, B. Y. Huang, E. Q. Xie, J. Y. Zhou and Z. X. Zhang, *Sens. Actuators, B*, 2015, **207**, 313–320.
- 40 C. D. Wagner, W. M. Riggs and L. E. Davis, *Standard ESCA spectra of the elements and line energy information*, Perkin-Elmer Corporation Physical Electronics Division, 1979.
- 41 M. Bagheri, A. A. Khodadadi, A. R. Mahjoub and Y. Mortazavi, *Sens. Actuators, B*, 2015, **220**, 590–599.
- 42 S. Park, S. Kim, G. L. Sun, S. Choi, S. Lee and C. Lee, *Ceram. Int.*, 2015, **41**, 9823–9827.
- 43 S. Park, H. Ko, S. An, W. I. Lee, S. Lee and C. Lee, *Ceram. Int.*, 2013, **39**, 5255–5262.
- 44 S. Park, S. Kim, G. J. Sun and C. Lee, *ACS Appl. Mater. Interfaces*, 2015, **7**, 8138–8146.
- 45 T. Zhang, F. B. Gu, D. M. Han, Z. H. Wang and G. S. Guo, *Sens. Actuators, B*, 2013, **177**, 1180–1188.
- 46 L. Zhang, F. B. Gu, Z. H. Wang, D. M. Han and G. S. Guo, *Key Eng. Mater.*, 2013, **562–565**, 543–548.
- 47 Y. D. Zhang, G. C. Jiang, K. W. Wong and Z. Zheng, *Sens. Lett.*, 2010, **8**, 355–361.
- 48 M. Chen, Z. H. Wang, D. M. Han, F. B. Gu and G. S. Guo, *Sens. Actuators, B*, 2011, **157**, 565–574.
- 49 X. Li, J. Liu, H. Guo, X. Zhou, C. Wang, P. Sun, X. Hu and G. Lu, *RSC Adv.*, 2015, **5**, 545–551.
- 50 A. Shanmugasundaram, B. Ramireddy, P. Basak, S. V. Manorama and S. Srinath, *J. Phys. Chem. C*, 2014, **118**, 6909–6921.